Neural Network-based Vegetation Attenuation Measurement and Modeling for Air-to-Ground Channels

Jiajia Zhou[1], **Ruonan Zhang**[1†], **Xiaoqian Yi**[2], **Marie Siew**[3], **Bin Li**[1], **Daosen Zhai**[1]

[1] School of Electronics and Information, Northwestern Polytechnical University, Xi'an, Shaanxi, China, 710129

[2]COMAC Flight Test Center, 108 Jinwen Road, Shanghai, China, 201323

[3]Pillar of Information Systems Technology and Design, Singapore University of Technology and Design, 8 Somapah Rd, Singapore, 487372

[†]rzhang@nwpu.edu.cn

Abstract

Vegetation, such as roadside trees and landscape forests, can obstruct the line-of-sight path between unmanned aerial vehicles (UAVs) and ground mobile terminals, causing fading in air-to-ground (A2G) communication links and significantly impacting the data rate and reliability of UAV communication and radio control systems. Therefore, accurate prediction of vegetation-induced fading is essential for UAV deployment and applications. This paper develops an A2G large-scale channel fading measurement system and conducts measurements and modeling across various regions and types of vegetation. According to the measurement results, we propose a vegetation attenuation prediction model based on a multilayer perceptron (MLP) for estimating attenuation in different scenarios. Experimental results demonstrate that, compared with the ITU-R model, the proposed model exhibits high prediction accuracy, offering an effective tool for optimizing UAV communication in vegetated environments.

1 Introduction

In recent years, unmanned aerial vehicles (UAVs), owing to their high mobility and rapid deployment capabilities, have shown great potential in applications such as emergency communications, disaster relief, and environmental monitoring (Tang et al. 2024). They are gradually becoming an essential component of future 6G space-air-ground integrated networks (Ge et al. 2022a). An accurate channel model serves as the fundamental basis for UAV communication system design. During the network planning stage, it provides essential references for link budget analysis, coverage estimation, and base station deployment (Sun et al. 2020). Channel models support the simulation and optimization of key algorithms such as beamforming and power control (Ge et al. 2022b).

Numerous researchers have conducted systematic channel measurement and modeling studies on A2G links in the Sub-6 GHz band, laying a solid foundation for understanding low-altitude communication propagation mechanisms. Yang et al.(2023) investigated the effect of UAV wobble on the temporal correlation of air-to-ground (A2G) wireless channels, revealing that even slight wobble can significantly alter the channel's temporal correlation. To address this, they proposed a non-stationary A2G channel model that accounts for UAV 3D wobble caused by both internal vibrations and atmospheric flow. This model contributes valuable insights for enhancing the design of UAV-based communication systems. Wang et al.(2019) conducted three-dimensional multipath measurements of a 3.5 GHz A2G link in a rural macrocell line-of-sight (LoS) scenario using a dual-channel MIMO sounder. The transmitting antenna was mounted on a UAV hovering at multiple altitudes, while a ground-based rectangular planar array received the signals and estimated the angles of arrival. The measurements revealed that as the UAV altitude increased, the azimuth angular spread decreased while the elevation angular spread increased. Based on these observations, a log-normal distribution model was established, highlighting the systematic differences in angular spread characteristics between air-to-ground and conventional terrestrial channels. Ge et al.(2021) conducted measurements of non-line-of-sight (NLoS) links at 5.8 GHz in a suburban low-altitude scenario, where the transmitter was placed on the rooftop of a high-rise building to emulate an aerial base station. Using a single-tone continuous wave system with omnidirectional antennas, the study revealed that clutter loss increases with decreasing elevation angle and decreases with increasing receiver height. Accordingly, elevation-angle-dependent models for clutter loss and path loss were proposed. Zhang et al.(2019) conducted dual-band A2G fading measurements at 785 MHz and 2160 MHz using a tethered balloon hovering at altitudes between 50 m and 950 m, while ground terminals moved along rural, suburban, and urban routes. Based on the measurement data, a path loss model incorporating carrier frequency, distance, and altitude correction factors was developed within the COST-2100 framework. Furthermore, they proposed a dual-band hybrid spectrum scheme, which significantly enhanced network throughput.

In low-altitude environments with vegetation on the ground, additional attenuation caused by tree obstruction and scattering leads to propagation characteristics that differ significantly from those in urban or open areas (Savage et al. 2003). Existing terrestrial channel models fail to accurately capture the propagation mechanisms of attenuation and scattering by ground vegetation. Therefore, conducting A2G channel measurement and modeling in representative vegetated environments is critical to support the

deployment of low-altitude A2G communication networks (Ndzi et al. 2012). Although the aforementioned studies provide valuable insights for A2G channel modeling, the additional attenuation caused by vegetation remains complex, being influenced by multiple coupled factors such as tree species, density, season, and frequency (He, Chen, and Jiang 2019). Numerous studies on vegetation attenuation modeling have been conducted to quantify and predict signal propagation loss characteristics in vegetated environments. Ogata et al.(2020) conducted outdoor measurements in forested areas of Japan during both summer and winter at three frequency bands—1.47, 3.35, and 5.77 GHz—using a UAV-mounted base station device and a vehicle-mounted omnidirectional antenna to establish a horizontally polarized link. The results showed that vegetation-induced excess loss was significantly higher in summer than in winter, with seasonal differences increasing by approximately 3 to 11 dB as frequency rose. Based on these findings, they proposed a seasonal vegetation loss model by incorporating frequency and month-dependent terms into the ITU-R P.833-9 framework. Xu et al.(2019) conducted propagation loss measurements of a 2.6 GHz cellular network in both dense and sparse vegetation scenarios over flat terrain in Yunnan, using Huawei terminals and drive-test software. The results indicated that signal loss in densely vegetated areas was significantly higher than in sparse regions. They proposed the TREENETs model as an extension of the standard propagation model, which substantially reduced prediction errors and proved effective for 5G base station planning. Montero et al.(2018) conducted UHF-band measurements at three tropical forest sites in Colombia, employing a transmitter–receiver comparison method to obtain differential measurements between obstructed and unobstructed links under both co- and cross-polarization conditions, thereby quantifying vegetation-induced excess loss. The results showed that attenuation was highly sensitive to vegetation type and vertical distribution. Within the FITU-R framework, they made parameter adjustments to propose an improved model adapted to local vegetation characteristics, resulting in significantly enhanced consistency across different scenarios.

Although existing vegetation attenuation models exhibit high prediction accuracy within their respective measurement scenarios, most of them are *developed based on terrestrial TX-to-RX links and have limited adaptability to different vegetation types and spatial distributions*, making them unsuitable for direct application in low-altitude UAV communication scenarios.

In this study, we **developed a low-altitude A2G channel measurement system**, and **conducted field measurements** across three representative vegetation-covered scenarios, encompassing multiple types of vegetation environments. During the measurements, the UAV, equipped with a transmitter, performed horizontal flights at altitudes of 30 m and 50 m, while a fixed ground receiver collected the signals, **yielding over 20000 valid samples** in total. The collected data comprehensively captured the statistical characteristics of vegetation-induced attenuation with respect to elevation angle, incidence depth, and relative distance, providing a solid empirical foundation for subsequent channel modeling and analysis.

This study first employed the traditional ITU-R empirical model for vegetation attenuation fitting. However, the resulting root mean square errors (RMSEs) were relatively large, indicating inaccuracies inherent in the fitting approach. To achieve more precise characterization of channel behavior and improve the prediction accuracy of vegetation attenuation, we developed **a vegetation attenuation prediction model based on a multilayer perceptron (MLP)**. The model takes channel parameters such as carrier frequency and transceiver elevation angle as input variables, enabling **adaptive learning of attenuation characteristics** under different vegetation environments. The proposed model demonstrated a significant reduction in RMSE across various measurement scenarios compared with traditional empirical models, validating the superiority of neural network-based methods for channel modeling in complex vegetated environments. Although the measurements were carried out at a center frequency of 4.95 GHz within the Sub-6 GHz range, the extracted attenuation statistics and the proposed modeling framework are expected to be extendable to neighboring Sub-6 GHz bands, with model parameters recalibrated using band-specific measurements when necessary.

The rest of the paper is organized as follows. Sec. 2 describes the channel sounder used in this campaign. The measurement scenario and procedure are presented in Sec. 3. Sec. 4 presents the measurement results and statistical analysis of vegetation incidence depth and vegetation attenuation. Sec. 5 proposes a vegetation attenuation prediction model based on a MLP and compares it with the ITU-R empirical model. Sec. 6 concludes the paper and points out future research issues.

2 Channel Measurement System

We developed a large-scale A2G channel measurement system for UAV communications, as illustrated in Fig. 1. The aerial transmitting unit consists of a DJI M100 UAV equipped with an RF module, antenna, and DC power supply, capable of ascending vertically to designated altitudes and performing horizontal movements. The ground receiving unit integrates a low-noise amplifier, spectrum analyzer, and data acquisition terminal to record the received signal power and GPS position information in real time.

The FPGA generates a digital sample sequence of a baseband tone signal, which is then converted to an analog signal using Direct Digital Synthesis (DDS) technology. The RF reconfigurable chip performs upconversion and shifts the baseband signal onto the desired RF frequency. The signal is subsequently transmitted through the RF port and an omnidirectional fiberglass antenna mounted vertically on the UAV.

The receiving antenna is vertically mounted on a height-adjustable support, and its type is identical to that of the transmitting antenna. The antenna is directly connected to a low-noise amplifier (LNA) to amplify the received signal. The amplified signal from the LNA output is fed via an RF cable to a signal analyzer for sampling the received

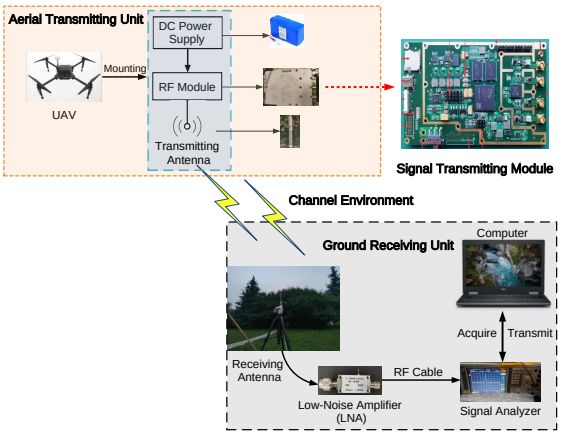

Figure 1: Architecture of the air-to-ground UAV channel measurement system.

signal power. The host computer connects to the signal analyzer through a local area network (LAN) interface, enabling real-time data acquisition and uploading. By calculating the difference between the transmitted power and the received power recorded by the signal analyzer, the signal attenuation during the measurement process can be obtained. To ensure accurate path loss calculation and minimize the impact of internal system factors on the results, we carefully calibrated the measurement system. During the channel measurement process, the received signal power obtained through over-the-air data acquisition can be expressed as (Wang, Sun, and Swindlehurst 2024):

$$P_r = P_t + G_t + G_r - G_{RFC} + G_{sys} - PL, \quad (1)$$

where P_r denotes the received power, P_t represents the transmitted power, G_t and G_r are the gains of the transmit and receive antennas, respectively, PL is the path loss experienced by the signal during propagation in the wireless channel, $G_{RFC}$and G_{ATT} represent the attenuation caused by the radio frequency cable and the attenuator, respectively. G_{sys} denotes the additional system gain or attenuation introduced by the TX-to-RX hardware.

We performed a direct connection calibration between the transmitter and receiver. The transmitted signal was routed through the same RF cable and a fixed-value attenuator directly from the transmitter's output port to the input port of the LNA at the receiver, while all other configurations remained unchanged. The received power under this condition, denoted as P_{dir}, can be expressed as:

$$P_{dir} = P_t - G_{RFC} - G_{ATT} + G_{sys}. \quad (2)$$

By subtracting Eq. (2) into Eq. (1), path loss in actual measurements can be calculated by:

$$PL = G_t + G_r + P_{dir} + G_{ATT} - P_r. \quad (3)$$

After averaging the results from the direct-connection calibration, we can determine the value of P_{dir}, while P_r corresponds to the received power from the valid sample data collected in the field measurement described above.

To verify the stability and accuracy of the measurement system, we conducted an experimental validation. We selected an open area where electromagnetic wave propagation could be approximated as free-space transmission. We placed the receiver at two distances from the transmitter—1 m and 10 m—and collected 10 samples at each position. The test frequency was set to 4.95 GHz, with both the transmit and receive antennas exhibiting a maximum gain of 2.6 dBi. Then we calculated path loss using (3) and compared the averaged measured values with the theoretical free-space path loss (FSPL) values. The theoretical FSPL can be expressed as:

$$PL = 20\lg d + 20\lg f - 20\lg\left(\frac{c}{4\pi}\right) - G_t - G_r, \quad (4)$$

where d denotes the relative distance between the transmitter and receiver, f represents the carrier frequency, and c is the speed of light. The comparison results show that when the receiver was placed 1 m from the transmitter, the measurement error was approximately 0.2411 dB, and when the distance increased to 10 m, the error was about 0.7361 dB. These results verify the accuracy and stability of the proposed measurement system, as the measured path loss closely matches the theoretical free-space model with errors below 1 dB over different distances. It confirms that the calibration effectively eliminates internal system biases and ensures reliable channel power measurements in subsequent experiments.

3 Channel Measurement Scenario

To comprehensively characterize the A2G channel propagation properties under different vegetation environments, we selected three representative measurement scenarios for field experiments. The measurement campaign was conducted on the campus of Northwestern Polytechnical University, located in the suburban area, where high-rise buildings are sparse and the terrain is open—features typical of a suburban communication scenario. Each measurement site consists of two consecutive vegetation-covered areas, denoted as *Area 1* and *Area 2*. The satellite images of the three selected measurement regions are shown in Figs. 3, 4, and 5, respectively. The measurement activity was carried out in August 2022, with the central frequency set to 4.95 GHz.

In Scenario 1, *Area A1* is a small plum garden approximately 32 m in length along the north–south direction, while *Area A2* is an artificial landscape forest about 394 m long, mainly consisting of willow and pine trees. The UAV carrying the transmitter flew from north to south, passing directly above *Area A1* and *Area A2*, with two flight missions conducted at altitudes of 30 m and 50 m. The receiver was positioned to the north of the plum garden at a height of 1.6 m, with a horizontal distance of 8.7 m from the boundary of *Area A1*.

In Scenario 2, *Area B1* primarily consists of low shrubs with an east–west length of approximately 7.7 m, while *Area B2* extends about 196 m and is covered by birch trees. The ground receiver was placed to the west of *Area B1* at a height of 1.1 m, with a horizontal distance of 1.7 m from the area. The UAV performed two flights from west to east at an altitude of 30 m.

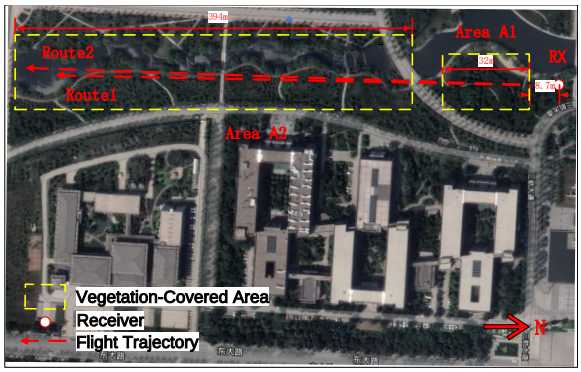

Figure 2: Satellite image of measurement scenario 1.

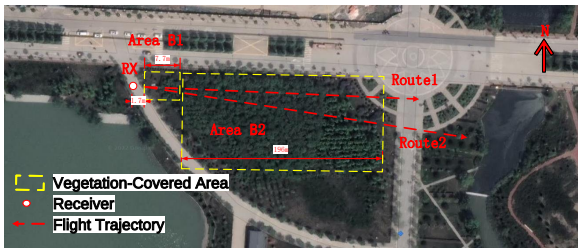

Figure 3: Satellite image of measurement scenario 2.

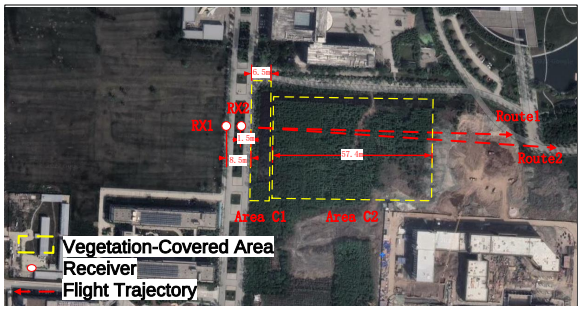

Figure 4: Satellite image of measurement scenario 3.

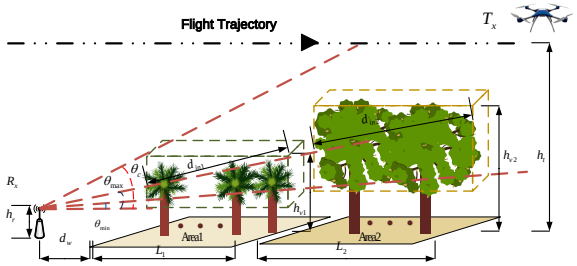

Figure 5: Geometric model of the vegetation attenuation measurement scenario.

In Scenario 3, *Area C1* consists of regularly arranged plane trees forming a roadside tree belt with a width of 8.5 m, while *Area C2* is a small maple forest approximately 57.4 m long in the east–west direction. The ground receiver was placed at two positions: *RX1* was located 8.5 m horizontally from *Area C1*, and *RX2* was positioned 2.5 m away, both at a height of 1.45 m. On the eastern side of *Area C2*, vegetation was sparse, allowing electromagnetic waves to propagate approximately in free space. The UAV conducted two flights from west to east at an altitude of 30 m.

During the measurement, the UAV flew at a constant speed along a predefined trajectory, while the ground receiver continuously collected and uploaded power measurements within a fixed frequency band. The sampling interval was set to 100 ms. Across six flight missions, a total of 7850, 6211, and 8698 valid sample points were collected in the three scenarios, respectively.

4 Measurement Results and Analysis

4.1 Vegetation Incidence Depth

To quantitatively analyze the propagation path length of electromagnetic waves penetrating vegetation, we establish a geometric model to calculate the vegetation incidence depth, as illustrated in Fig. 5. In the model, h_r and h_t denote the heights of the receiving and transmitting antennas, respectively. *Area 1* and *Area 2* represent two vegetation-covered regions. L_1 and L_2 denote the horizontal lengths of these two areas, d_w represents the horizontal distance between the receiver and the forested region, h_{v1} and h_{v2} are the average tree heights in *Area 1* and *Area 2*, respectively, and d_{in1} and d_{in2} correspond to the vegetation incidence depths of the signal within the two forested areas during propagation.

Based on geometric principles, the vegetation incidence depths can be calculated by:

$$d_{in} = \begin{cases} 0, & \theta \geq \theta_c, \\ \frac{h_{vi} - d'_w \cdot \tan\theta - h_r}{\sin\theta}, & \theta_{\max} \leq \theta < \theta_c, \\ \frac{L_i}{\cos\theta}, & \theta_{\min} < \theta < \theta_{\max}, \\ L_i, & \theta \leq \theta_{\min}, \end{cases} \tag{5}$$

where θ denotes the elevation angle of the LoS path between the receiver and the transmitter, and θ_c represents the critical angle at which the direct path between the UAV and the receiver becomes just obstructed by the tree canopy during horizontal flight. The critical angle can be calculated by:

$$\theta_c = \arctan \frac{h_{vi} - h_r}{d'_w}, \tag{6}$$

where h_{vi} denotes the average tree height within the i-th vegetation-covered area, and d'_w represents the horizontal distance from the receiver to that area. $\theta_{\max}$ denotes the angle at which the vegetation incidence depth along the propagation path reaches its maximum value:

$$\theta_{\max} = \arctan \frac{h_{vi} - h_r}{d'_w + L_i}, \tag{7}$$

where L_i denotes the horizontal length of the i-th area. As the UAV flies and the TX-to-RX elevation angle exceeds $\theta_{\max}$, the vegetation incidence depth gradually decreases. $\theta_{\min}$ represents the critical angle at which the tree canopy just does not obstruct the slant propagation path between the

		Scenario		
		1	2	3
θ (°)	Route1	60.37–3.83	70.92–4.39	55.83–8.44
	Route2	85.40–5.37	70.92–5.11	82.60–9.28
d_{in} (m)	Route1	0–180.78	0–132.81	0–41.71
	Route2	0–117.27	0–132.81	0–41.71

Table 1: Calculation results of TX-to-RX elevation angles and vegetation incidence depths under different scenarios.

transmitter and receiver:

$$\theta_{\min} = \arctan\frac{(1-K)\cdot h_{vi} - h_r}{d'_w + L_i}, \tag{8}$$

where K denotes the average canopy ratio within the area, defined as the ratio of the tree canopy width to the average tree height. Theoretically, dense branches and leaves within the canopy are the primary sources of signal attenuation. However, when $\theta < \theta_{\min}$, although only the tree trunks obstruct the direct signal path, attenuation of the electromagnetic wave still occurs but increases very slowly. Therefore, the incidence depth is treated as a constant, equal to the horizontal length of the current area.

Based on the real-time GPS information of the UAV and the aforementioned geometric model, we calculate the elevation angle and vegetation incidence depth along different UAV flight trajectories for the three measurement scenarios. The detailed results are presented in Table 1.

4.2 Vegetation Attenuation

The impact of all ground-based scatterers on signal propagation can be quantified by subtracting the FSPL from the actual measured path loss along the same propagation path(Bertoni 1999), as expressed by:

$$\begin{aligned} L_{\text{clu}} &= PL - PL_{\text{free}} \\ &= PL - 32.44 - 20\log_{10}(d_{\text{3D}}) - 20\log_{10}(f_c), \end{aligned} \tag{9}$$

where PL_{free} represents the FSPL in dB, d_{3D} denotes 3D relative distance between the unmanned aerial vehicle and the ground receiver (m), and f_c is the carrier frequency (GHz).

Since the selected measurement areas and UAV flight trajectories are located far from buildings and other man-made structures, with flights conducted only above vegetation-covered regions, the ground-induced loss can be attributed solely to the vegetation within the measurement area. Therefore, the attenuation can be equivalently represented by $L_v = L_{clu}$ given in (9).

Based on geometric relationships, it can be concluded that in Scenario 1, when the direct propagation path is fully blocked by the vegetation in *Area 1*, the critical elevation angle $\theta_{c1} = 42.60°$. If the influence of *Area 1* is ignored, the direct path is fully obstructed by the vegetation in *Area 2* at the critical elevation angle $\theta_{c2} = 19.98°$. Fig. 6 illustrates the variation of vegetation attenuation with elevation angle in Scenario 1 (only showing the scenarios with vegetation attenuation). It can be observed that as the elevation angle decreases from 42.60° to 19.98°, the vegetation attenuation increases slowly, fluctuating around 5 dB. After the elevation angle reaches 19.98°, the vegetation attenuation increases rapidly, with the fluctuation from 10 dB to 40 dB. However, the overall trend still shows that the vegetation attenuation increases gradually as the elevation angle decreases.

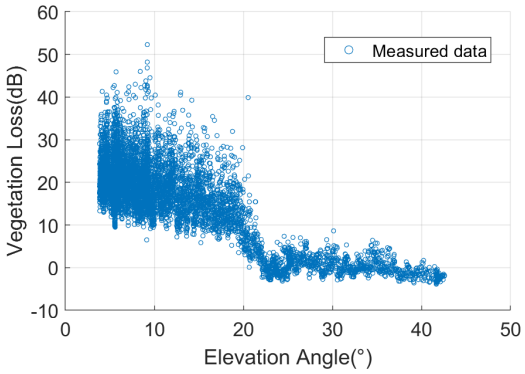

Figure 6: Variation of vegetation attenuation with elevation angle in scenario 1.

Scenario	**1**	**2**	**3**
Vegetation Type	Plum, Willow, Pine	Shrubs, Birch	Phoenix Tree, Maple
A	0.4913	0.3067	0.05405
B	-0.1116	0.1683	0.5516
C	0.7311	0.6101	0.3933
E	0.5734	0.1777	0.7993
G	0.6037	0.6310	-0.1193

Table 2: Empirically fitted parameters for different vegetation types under various scenarios for ITU-R model.

5 Channel Modeling

5.1 ITU-R Empirical Fitting Model

To characterize the vegetation attenuation observed in different scenarios, we first adopted the traditional ITU-R empirical model as a baseline for curve fitting. The mathematical form of the ITU-R empirical model is (ITU-R P.833-10 2021):

$$L_v = Af^B d^C(\theta + E)^G, \tag{10}$$

where L_v denotes the vegetation attenuation (dB), f is the carrier frequency (MHz), d is the vegetation penetration depth (m), θ is the elevation angle of the transmitter and receiver (°), and A, B, C, E, and G are empirically derived parameters. These parameters can be fitted based on measured values in different communication environments and are influenced by the types of vegetation. The fitted values of the empirical parameters for the three scenarios are shown in Table 2, indicating significant differences among the scenarios.

To evaluate the modeling performance, we calculated the root mean square error (RMSE) for the empirical fitting models, given by:

$$X_{\text{RMSE}} = \sqrt{\frac{\sum_{i=1}^{N_k}(\hat{L}_i - L_i)^2}{N_k}}, \quad k = 1, 2, 3, \tag{11}$$

Scenario	Scenario 1	Scenario 2	Scenario 3
X_{RMSE} (dB)	8.4276	21.7149	7.0860

Table 3: RMSE values of the fitted models for the three measurement scenarios.

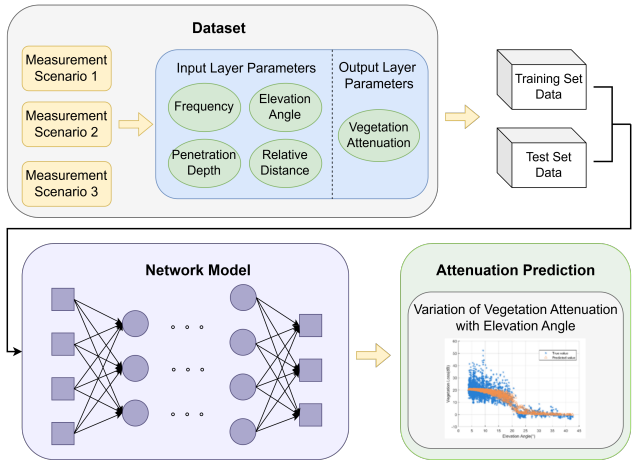

Figure 7: Schematic diagram of the vegetation attenuation prediction model based on multi-layer perceptron.

where N_k represents the number of the data samples used for model fitting in the three measurement scenarios, L_i is the actual measured value of vegetation loss, and $\hat{L}_i$ denotes the predicted value obtained from the fitted model.

The RMSEs for the three scenarios are listed in Table 3. The relatively large RMSEs indicate that the fitting method based on the ITU-R empirical model contains errors. It suggests that this approach cannot accurately characterize the impact of the vegetation environment on signal attenuation.

5.2 Neural Network–Based Attenuation Prediction Model

To overcome the limitations of the ITU-R empirical fitting model and more comprehensively describe the statistical characteristics of the large-scale fading in vegetation environments, this paper proposes a vegetation attenuation prediction model based on a MLP neural network. A schematic diagram of the model structure is shown in Fig. 7.

We adopted a 4-layer neural network architecture to improve iteration efficiency (Singh and Banerjee 2019). Channel measurements were conducted in three different scenarios, resulting in a total of 20675 propagation attenuation data samples. The dataset was split into training and test sets with a ratio of 70% and 30%, respectively. The input features for the MLP include carrier frequency, vegetation penetration depth, elevation angle, and relative distance, while the output is the predicted value of vegetation attenuation. Given the moderate feature dimensionality and sample size, a deeper or more sophisticated architecture may offer limited additional gain while substantially increasing the model complexity and overfitting risk. The specific settings for the model's hyperparameters are provided in Table 4.

Parameter Name	Parameter Value
Number of Network Layers	4
Number of Input Neurons	4
Number of Output Neurons	1
Training Set Samples	14472
Test Set Samples	6203
Batch Size	64
Number of Subsets	227
Activation Function	Sigmoid
Loss Function	Mean Squared Error (MSE)
Epochs	50
Learning Rate	0.05
Gradient Update Algorithm	Adaptive Moment Estimation (Adam)

Table 4: Configuration of multi-layer perceptron neural network parameters.

To ensure a reasonable range of variation in the training data, we first applied the min–max normalization method for data standardization. The cost function of the output layer for all samples is related to the weights and biases (Tang et al. 2025):

$$E(\mathbf{W},\mathbf{b}) = \frac{1}{N}\sum_{i=1}^{N} e(\hat{y}_i, y_i) = \frac{1}{2N}\sum_{i=1}^{N}(\hat{y}_i - y_i)^2, \quad (12)$$

where $\mathbf{W}$ and $\mathbf{b}$ represent the weight and bias matrices, respectively, N is the number of samples in the training set, $\hat{y}_i$ is the predicted output for the i-th sample, and y_i is the target value for the i-th sample.

To further improve the training efficiency, we adopted the mini-batch gradient descent method to optimize the training process. In this model, we employed the Adam optimization algorithm to update the weight and bias matrices. The computation process is as follows:

$$\begin{aligned}
\mathbf{W}(k+1) &= \mathbf{W}(k) - \alpha\Delta\mathbf{W}(k) \\
&= \mathbf{W}(k) - \alpha\frac{\mathbf{V}_{d\mathbf{W}}^{corrected}(k)}{\sqrt{\mathbf{S}_{d\mathbf{W}}^{corrected}(k)+\varepsilon}}, \\
\mathbf{b}(k+1) &= \mathbf{b}(k) - \alpha\Delta\mathbf{b}(k) \\
&= \mathbf{b}(k) - \alpha\frac{\mathbf{V}_{d\mathbf{b}}^{corrected}(k)}{\sqrt{\mathbf{S}_{d\mathbf{b}}^{corrected}(k)+\varepsilon}},
\end{aligned} \quad (13)$$

where $\mathbf{V}_{d\mathbf{W}}$ and $\mathbf{S}_{d\mathbf{W}}$ denote the first- and second-order biased moment estimates of the weight matrix, respectively, $\mathbf{V}_{d\mathbf{b}}$ and $\mathbf{S}_{d\mathbf{b}}$ represent the first- and second-order biased moment estimates of the bias matrix. k is the iteration index, α denotes the learning rate, and ε is a small constant introduced to ensure numerical stability, typically set to 10^{-8}.

The variation of the loss function during training is illustrated in Fig. 8. It can be observed that the loss function decreases with fluctuations as the number of iterations increases. During the first 2000 iterations, the loss decreases significantly from approximately 10^{-1} to 10^{-2}. In the subsequent training process, the loss fluctuates between 10^{-2} and 10^{-3}, with the error maintained within the range of about 1% to 0.1%. This indicates that the model gradually achieves a stable and satisfactory fitting performance.

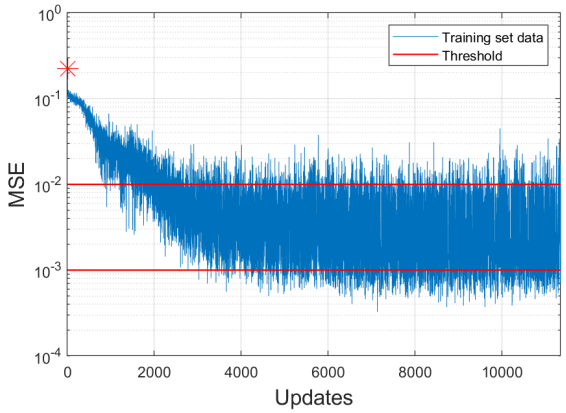

Figure 8: Variation of the loss function with the number of iterations.

		Scenario		
		1	2	3
X_{RMSE} (dB)	MLP	5.3610	3.6158	4.3144
	ITU-R	8.4276	21.7149	7.0860

Table 5: RMSE comparison between the MLP model and the ITU-R model across the three measurement scenarios.

To verify the prediction accuracy of the proposed model, the test set were fed into the network after training to obtain the predicted values, which were then compared with the actual measurements. Fig. 9 illustrates the actual vegetation attenuation and the predicted values in different measurement scenarios. It can be observed that in Scenarios 1 and 2, when the transceiver elevation angle is relatively high, the predicted values closely match the actual measurements. However, at lower elevation angles, the raw measurement data become more scattered and exhibit greater variability, resulting in more concentrated predicted values and correspondingly higher RMSE. In Scenario 3, certain discrepancies can be observed between the predicted and actual vegetation attenuation values at different receiver positions. The predicted values can fully capture the variation trend of the actual measurements over the elevation angle ranges, and the model demonstrates satisfactory prediction accuracy, indicating its strong adaptability and effectiveness.

Table 5 presents the RMSEs between the actual electromagnetic wave propagation loss and the predicted values in the three measurement scenarios using the test dataset. It can be observed that, compared with the ITU-R model, the proposed MLP model exhibits a significant improvement in fitting performance for all scenarios, with enhancements of approximately 3.1 dB, 18.1 dB, and 2.8 dB, respectively. Notably, the prediction accuracy of the model improves substantially in Scenario 2.

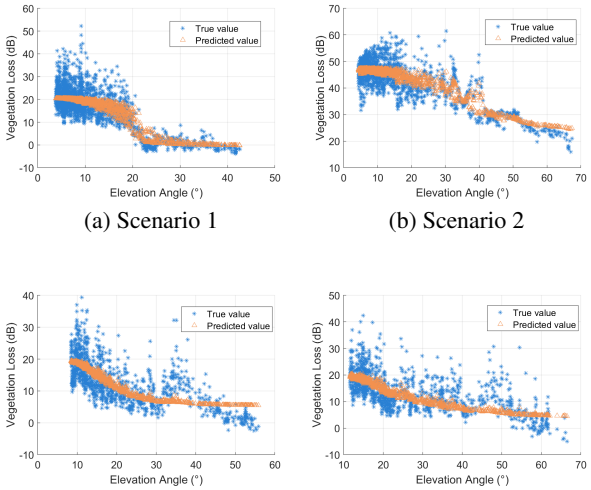

(a) Scenario 1 (b) Scenario 2

(c) Scenario 3 RX1 (d) Scenario 3 RX2

Figure 9: Comparison between measured and predicted vegetation attenuation under different scenarios.

6 Conclusions

In this study, we developed an A2G large-scale fading measurement system, and conducted channel measurements across different regions and vegetation types. The MLP-based vegetation attenuation prediction model proposed in this paper can be effectively applied to wireless channel modeling in complex vegetation environments. By incorporating multidimensional features such as carrier frequency, penetration depth, and elevation angle, the model successfully captures the statistical characteristics of vegetation-induced attenuation and achieves significantly higher prediction accuracy compared with the ITU-R empirical model. This study provides a new neural network–based approach for channel characterization in vegetated environments and offers valuable insights for the design of wireless communication systems in complex scenarios such as forests and mountainous areas. Future work may extend the study to different frequency bands and more diverse vegetation types, and further incorporate small-scale fading characteristics to develop a more comprehensive vegetation attenuation channel model.

Acknowledgments

This work was supported in part by the National Natural Science Foundation of China (No. 62232013 and No. 62171385) and in part by the China Scholarship Council (CSC).

References

Bertoni, H. L. 1999. *Radio propagation for modern wireless systems*. Pearson Education.

Ge, C.; Zhang, R.; Jiang, Y.; Li, B.; and He, Y. 2022a. A 3-D dynamic non-WSS cluster geometrical-based stochas-

tic model for UAV MIMO channels. *IEEE Transactions on Vehicular Technology*, 71(7): 6884–6899.

Ge, C.; Zhang, R.; Yang, Y.; Jiang, Y.; and Li, B. 2021. Clutter loss of low-altitude UAV channel in suburban scenario at 5.8 GHz. *IEEE Antennas and Wireless Propagation Letters*, 21(4): 651–655.

Ge, C.; Zhang, R.; Zhai, D.; Jiang, Y.; and Li, B. 2022b. UAV-correlated MIMO channels: 3-D geometrical-based polarized model and capacity analysis. *IEEE Internet of Things Journal*, 10(2): 1446–1460.

He, F.; Chen, J.; and Jiang, C. 2019. Surface wave attenuation by vegetation with the stem, root and canopy. *Coastal Engineering*, 152: 103509.

ITU-R P.833-10. 2021. Attenuation in Vegetation. Recommendation. Available at: https://www.itu.int/rec/R-REC-P.833-10-202109-I/en.

Montero, O.; Pantoja, J. J.; Patiño, M.; Pineda, E.; Martinez, D.; Angel, G.; Cruz, J.; Suarez, M.; and Vega, F. 2018. Attenuation of Radiofrequency Waves due to Vegetation in Colombia. In *2018 IEEE-APS Topical Conference on Antennas and Propagation in Wireless Communications (APWC)*, 940–943. IEEE.

Ndzi, D. L.; Kamarudin, L. M.; Ezanuddin, A. A. M.; Zakaria, A.; Ahmad, R. B.; Abd Malek, M. F. B.; Shakaff, A. Y. M.; and Jafaar, M. 2012. Vegetation attenuation measurements and modeling in plantations for wireless sensor network planning. *Progress In Electromagnetics Research B*, 36: 283–301.

Ogata, D.; Sato, A.; Kimura, S.; and Omote, H. 2020. A study on vegetation loss model with seasonal characteristics. In *2020 14th European Conference on Antennas and Propagation (EuCAP)*, 1–4. IEEE.

Savage, N.; Ndzi, D.; Seville, A.; Vilar, E.; and Austin, J. 2003. Radio wave propagation through vegetation: Factors influencing signal attenuation. *Radio Science*, 38(5): 9–1.

Singh, J.; and Banerjee, R. 2019. A study on single and multi-layer perceptron neural network. In *2019 3rd International Conference on Computing Methodologies and Communication (ICCMC)*, 35–40. IEEE.

Sun, L.; Wang, Y.; Swindlehurst, A. L.; and Tang, X. 2020. Generative-adversarial-network enabled signal detection for communication systems with unknown channel models. *IEEE Journal on Selected Areas in Communications*, 39(1): 47–60.

Tang, X.; Xiong, Z.; Dong, L.; Zhang, R.; and Du, Q. 2024. UAV-enabled aerial active RIS with learning deployment for secured wireless communications. *Chinese Journal of Aeronautics*, 103383.

Tang, X.; Zhao, K.; Shen, C.; Du, Q.; Wang, Y.; Niyato, D.; and Han, Z. 2025. Deep Graph Reinforcement Learning for UAV-Enabled Multi-User Secure Communications. *IEEE Transactions on Mobile Computing*.

Wang, Y.; Sun, L.; and Swindlehurst, A. L. 2024. Knowledge-driven signal detector for uplink transmission in IoT networks with unknown channel models. *IEEE Internet of Things Journal*, 11(15): 25839–25852.

Wang, Y.; Zhang, R.; Li, B.; Tang, X.; and Wang, D. 2019. Angular spread analysis and modeling of UAV air-to-ground channels at 3.5 GHz. In *2019 11th International Conference on Wireless Communications and Signal Processing (WCSP)*, 1–5. IEEE.

Xu, L.; Zhang, J.; He, X.; Jing, Y.; and He, W. 2019. Influence of Vegetation Coverage on Radio Wave Propagation Loss at 2.6 GHz. In *2019 IEEE 4th Advanced Information Technology, Electronic and Automation Control Conference (IAEAC)*, volume 1, 657–661. IEEE.

Yang, X.; Zhai, D.; Zhang, R.; Liu, L.; Yu, F. R.; and Leung, V. C. 2023. Temporal correlation characteristics of air-to-ground wireless channel with UAV wobble. *IEEE Transactions on Intelligent Transportation Systems*, 24(10): 10702–10715.

Zhang, R.; Guo, Q.; Zhai, D.; Zhou, D.; Du, X.; and Guizani, M. 2019. Channel measurement and resource allocation scheme for dual-band airborne access networks. *IEEE Access*, 7: 80870–80883.